



A hierarchical dual-phase photoetching template route to assembling functional layers on Si photoanode with tunable nanostructures for efficient water splitting

Yang Li^a, Guangzhou Xu^b, Xinyue Zhu^a, Zaiqin Man^a, Xinxin Fu^a, Zongbin Hao^a, Yushuang Cui^a, Changsheng Yuan^a, Weihua Zhang^a, Shicheng Yan^{b,*}, Haixiong Ge^{a,*}, Yanfeng Chen^a, Zhigang Zou^c

^a Department of Materials Science and Engineering, College of Engineering and Applied Sciences, Nanjing University, Nanjing, Jiangsu 210093, PR China

^b Jiangsu Key Laboratory of Artificial Functional Materials, Eco-materials and Renewable Energy Research Center (ERERC), Collaborative Innovation Center of Advanced Microstructures, College of Engineering and Applied Sciences, Nanjing University, No. 22, Hankou Road, Nanjing, Jiangsu 210093, PR China

^c Jiangsu Key Laboratory for Nano Technology, National Laboratory of Solid State Microstructures, Department of Physics, Nanjing University, No. 22, Hankou Road, Nanjing, Jiangsu 210093, PR China

ARTICLE INFO

Keywords:

Hierarchical dual-phase mask
Surface modification
Photoelectrochemistry
Si photoanode
Water splitting

ABSTRACT

Surface functionalization is closely associated with the light harvesting and the charge separation, transfer, and injection efficiencies of water-splitting photoelectrode. Here, a dual-phase photoetching template with hierarchical structure, polyphenylsilsequioxane nanopillars and bicontinuous polyphenylsilsequioxane + polystyrene network layer, is patterned on the Si photoanode via a spinodal phase separation mechanism. Controllably photoetching the polymer template allows us to physically deposit functional layers with tunable nanostructures from net to dispersed dot. As a demonstration, the broken Ni/NiO_x net modified Si photoanode exhibits a low onset potential of 0.93 V_{RHE}, a high saturated photocurrent density of 40 mA cm⁻² and a stability of 50 h in 1.0 M K-borate under AM1.5 G illumination, resulting from the inhomogeneous barrier height driven efficient charge extraction and low light loss by the dispersed surface modification. The proposed dual-phase lithographic template may open a new avenue to easily assemble functional layers on photoelectrodes for efficient solar energy conversion.

1. Introduction

Nowadays, photoelectrochemical (PEC) water splitting is considered to be a promising approach to split water, generating clean H₂ fuel directly from solar energy [1–3]. A highly efficient PEC cell requires fast charge separation and transfer at the semiconductor-electrolyte interface, efficiently harvesting the sunlight, and long-term stability [4,5]. Silicon (Si) is deemed as one of the most attractive materials on account of its abundance, low cost, high carrier mobility, and excellent ability to absorb sunlight with a narrow band gap (1.1 eV) [6,7]. However, Si is very prone to be oxidized to insulating SiO_x by photo/or electrochemical corrosion during the illumination. In particular, the corrosion of photoanode is serious due to the sluggish oxygen evolution reaction (OER) with 4-electron transfer process [8,9]. Hence, a corrosion-resistant layer with high light transmissivity, excellent conductivity, and good catalytic activity for water splitting, is highly

desired.

The various materials, such as TiO_x/Co-Pi [10], CoO_x [11], Ni [12], ITO/NiO_x [13], and NiFe(OH)_x [14], were densely coated on Si surface as a functional layer to retard corrosion, extract charge, and accelerate water oxidation. Dense layers usually induce the shading effect due to the light loss in these layers. Dispersing the nanoparticles on the Si electrodes is an effective strategy to achieve the high light harvesting, efficient charge extraction, and low barrier for water splitting [15,16]. The electrochemically dispersed nanoparticles, such as Ni/NiO_x [17], Co [18], NiFe alloys [19], and Ni@Ni(OH)₂ [20], were exemplified to be the efficient charge collector with the minimizing light loss, thus affording highly efficient solar water splitting. The reactively sputtering, atomic-layer deposition, and electrodeposition are the popular techniques to coat the functional layers onto the Si surface. However, a challenge in use of these techniques is to control the microstructure, even to form the dispersed nanoparticles for minimizing the shading

* Corresponding authors.

E-mail addresses: yscfei@nju.edu.cn (S. Yan), haixiong@nju.edu.cn (H. Ge).

<https://doi.org/10.1016/j.apcatb.2019.118115>

Received 19 July 2019; Received in revised form 19 August 2019; Accepted 22 August 2019

Available online 23 August 2019

0926-3373/ © 2019 Elsevier B.V. All rights reserved.

effect. This situation hinders understanding the PEC mechanism for water splitting over the dispersed functional particles on the Si electrodes.

Herein we proposed a general dual-phase photoetching template to assemble functional layers on Si electrodes. By using spin coating technique, a dual-phase polymer photoetching template of polyphenylsilse quioxane (PPSQ) and polystyrene (PS) was patterned on the Si photoanode via a spinodal phase decomposition mechanism. The generated template was composed of a hierarchical structure of PPSQ nanopillars and bicontinuous PPSQ + PS network. Selectively etching the patterns of PPSQ and PS allows us to deposit multifunctional layers with tunable nanostructures onto surface of Si electrodes. As a typical example, Ni was patterned on the Si surface with easily tuning nanostructures from the continuous net to the dispersed nanoparticles. More importantly, the proposed route is also suitable to produce the composite layers by the physical vapor deposition. As a demonstration, the Ni/NiO_x broken nanonets modified Si photoanode exhibited a low onset potential of 0.93 V vs. reversible hydrogen electrode, a high saturated photocurrent density of 40 mA cm⁻² and a stability of 50 h in 1.0 M K-borate under AM 1.5 G illumination. The facilely tuning microstructures offer a chance to deeply understand the mechanism of charge separation and transfer at semiconductor/electrolyte interface after modification by functional layers with different microstructures. We found that the dispersed nanoparticles on Si surface may induce the inhomogeneous barrier height driven efficient charge extraction, greatly contributing to the high PEC performance. Our proposed dual-phase lithographic template may open a new avenue to easily assemble functional layers on photoelectrodes for efficient solar energy conversion.

2. Results and discussion

2.1. Strategy for patterning multifunctional layers with tunable nanostructures on Si electrodes

As described in Fig. 1a, a three-layer photoetching template was coated on the surface of Si. A 200 nm-thick poly(methyl methacrylate) (PMMA), as lifting-off layer for easily removing by organic cleaning solvent, was first formed on the Si substrate by spin coating. After that, a 20 nm-thick SiO₂, as isolating layer to prevent the PMMA from dissolving by toluene that is used as the solvent of PS and PPSQ, was coated on PMMA layer by plasma enhanced chemical vapor deposition (PECVD). Finally, a 180 nm-thick PPSQ + PS dual-phase mask layer was spin-coated onto the SiO₂ layer by using the polymer solution that was prepared by dissolving PS and PPSQ into toluene. During the spin coating, volatilizing of the toluene results in phase separation of PPSQ and PS to generate a dual-phase mask layer.

Scanning electron microscopy (SEM) observations indicated that the PPSQ nanopillars with about 100–500 nm diameter were alternately inlaid in PS phase (Fig. 1b). The phase separation between two immiscible polymers, PPSQ and PS, would follow the spinodal decomposition mechanism during the evaporation of solvent [21,22]. This phase transformation was achieved by an uphill diffusion process to generate the PS-rich and PPSQ-rich regions in the final product, that is, both the PPSQ and PS diffuse from the low-concentration region to the high-concentration region, driving by the composition fluctuation during the evaporation of solvent. Such a domain structure for inlaying the PPSQ pillars into the PS bulk depends on the relative solubility of the two polymers in toluene solvent. Toluene is a better solvent for PS than for PPSQ. During the phase separation, the PS-rich phase contains more toluene than the PPSQ phase and the PPSQ is more quickly depleted of the solvent and solidifies earlier than the PS. Subsequently, the evaporation of the remaining solvents leads to a further collapse of high-solubility PS phase to coat the PPSQ pillars. Usually, the periodic composition fluctuation occurs in a given microdomain, thus producing the nearly ordered PPSQ patterns.

After the O₂ reactive-ion etching (RIE), the PS constituent was selectively removed due to the high etching resistance of PPSQ. Obviously, an about 50 nm-thick worm-like PPSQ + PS interconnected network layer was observed in the space among the PPSQ pillars on the surface of SiO₂ layer (Fig. 1c and d). Unlike the PPSQ pillars, the worm-like PPSQ network layer stopped growing next to about 50 nm on surface of SiO₂, probably implying a different spinodal process by surface effects. The surface of SiO₂ layer is hydrophilic. In our previous report [21], we have found that compared to PS the PPSQ exhibited a stronger wettability on Si surface, meaning a stronger polarity for PPSQ than PS. As a result, the PPSQ tends preferentially to adsorb onto the surface of hydrophilic SiO₂. Such a strong interaction between PPSQ and SiO₂ may decay the lateral diffusion of PPSQ, producing a bicontinuous PS + PPSQ layer. Indeed, it was well demonstrated that surface effects may lead to physical properties that significantly differ from those in bulk [23,24]. Therefore, the frustrated diffusion process rapidly disappeared when the surface interactions are much too weak at a region far from the SiO₂ surface. Such a composite polymer template with a hierarchical structure gives us a possibility to tune its microstructure by photoetching due to the big differences in etching resistance of PS and PPSQ and in particle size of PPSQ pillars and PPSQ + PS network. As shown in Fig. 2, the PS phase can be completely removed from the overlayer of mask template by O₂ RIE with an etching rate of 1.01 nm/s, thus keeping the PPSQ pillars and bicontinuous PS + PPSQ network layer (Fig. 2a). Subsequently, the CHF₃/O₂ RIE was used to etch the PPSQ nanopillars and bicontinuous PS + PPSQ network layer. By using the CHF₃/O₂ RIE, the removal rate is much faster for PS (1.37 nm/s) than PPSQ (0.27 nm/s). Therefore, we can control the etching time to form the specific pores in the about 50 nm-thick bicontinuous PS + PPSQ layer on the surface of SiO₂ and keep the PPSQ pillars as a mask resulting from their big particle size (about 180 nm in height and 100–500 nm in diameter) enough to resist the photoetching. Then, the tailored bicontinuous layer could be used as the second mask template to respectively etch the SiO₂ layer by the CHF₃/CHF₄ RIE (0.20 nm/s) and the PMMA layer by O₂ RIE (2.5 nm/s), thus fabricating a through-hole reaching to the surface of Si substrate. Small isolated pores, isolated worm-like pores, and connected macropores were formed by CHF₃/O₂ RIE to etch the bicontinuous PS + PPSQ network layer for a short (about 60 s, mainly removing the PS), medium-scale (about 120 s, removing the PS + partial PPSQ network), and long (about 160 s, completely removing the PS + PPSQ network) etching times, respectively. The functional materials were deposited into these pores and patterned on the surface of Si after lifting off the residual polymer layer by organic solvent. As a typical example, using the tailored template, we patterned a 5 nm-thick Ni layer by physical vapor deposition (PVD) on the Si substrate. After lifting-off the PMMA layer by acetone, the dispersed Ni dot (Fig. 2b), broken Ni net (Fig. 2c), and continuous Ni net (Fig. 2d) were respectively obtained by using the templates generated from short, medium-scale, and long etching time. The proposed method is also suitable to produce the composite layers, such as Ni/NiO_x, with precisely controlled thicknesses by the PVD process.

In addition, the feature size of PPSQ nanopillars is sensitive to the phase separation parameters such as the polymer ratio, the solution concentration, and the spinning speed [21]. Particularly, higher solution concentration may lead to longer evaporation time of toluene, and thus may provide more time for dispersed PPSQ phase to coalesce and grow into larger domains, resulting in larger feature sizes of PPSQ nanopillars. Thus, when using a template with complete removal of bicontinuous PS + PPSQ layer, the duty ratio of Ni nanonets increased from 38%, to 42%, and to 62% due to the reduced lateral size of PPSQ nanopillars by decreasing the weight ratio of solute (PS + PPSQ) to solvent (toluene) from 5 wt.%, to 4 wt.%, and to 3 wt.% (Fig. S1, Supporting Information). These results indicated that the dual-phase photoetching template with a hierarchical structure allows us to pattern the functional layer with various microstructures on Si substrate by facilely

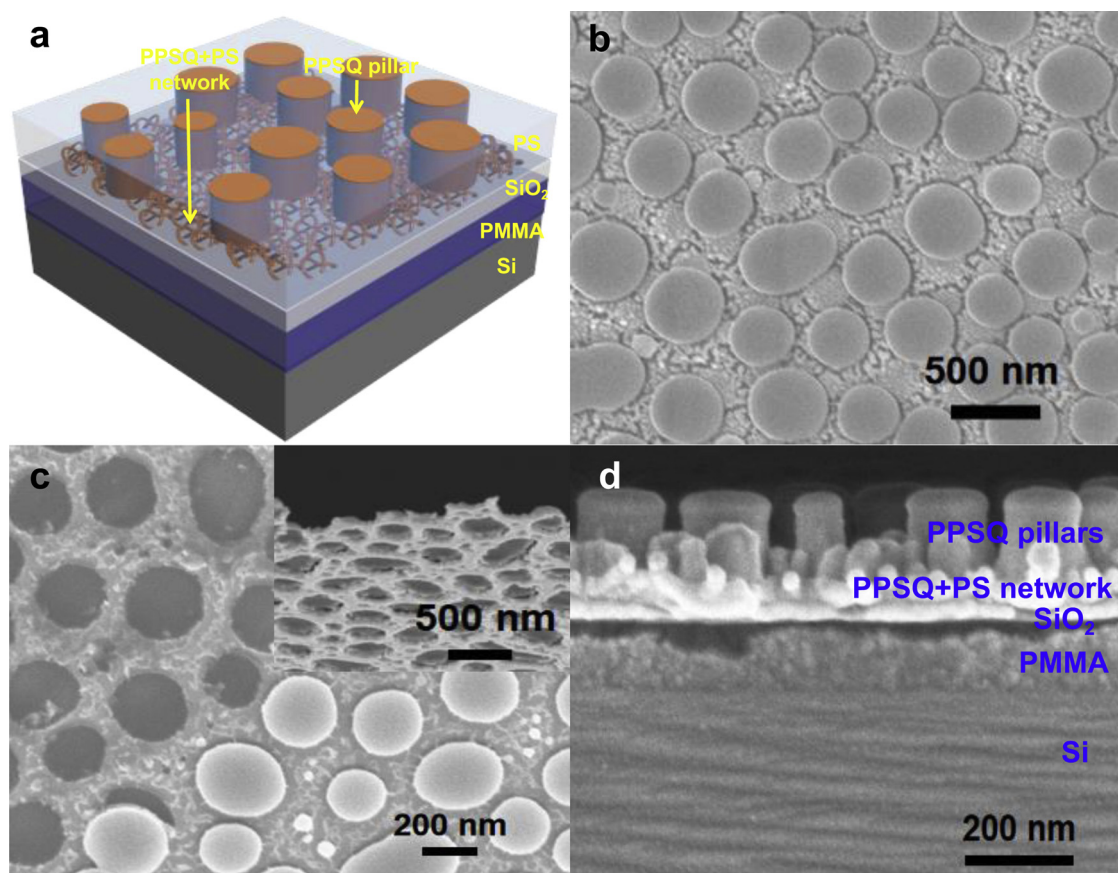


Fig. 1. a) A schematic diagram showing the three-layer mask template on Si substrate. PMMA lifting-off layer, SiO₂ isolating layer, PS + PPSQ mask layer were in turn coated on the Si substrate. Noting that the mask layer composed of a hierarchical structure, the PPSQ pillar + PS layer and the bicontinuous PPSQ + PS network layer, which respectively formed by a spinodal decomposition mechanism and a surface interaction inducing spinodal decomposition mechanism. b) A top-view SEM image shows that the PPSQ pillars were inlaid in PS bulk. c) A top-view SEM image to exhibit the worm-like PPSQ + PS network layer on surface of SiO₂ layer, resulting from a surface interaction effects inducing spinodal phase separation mechanism. Inset shows the bicontinuous PPSQ + PS network layer which was peeled from the surface of SiO₂ layer. d) A cross-section SEM image of the three-layer template with a hierarchical PS + PPSQ mask layer.

tuning the solute-solvent ratio of dual-phase polymer precursors and photoetching parameters.

2.2. PEC performance of n-Si electrodes with broken Ni/NiO_x net, broken Ni net or Ni net

To figure out the effects of 5 nm-thick Ni layer on photoelectrochemical (PEC) performances of Si photoanodes, the coverage rate of Ni layer was varied from 100% to 1.5% (Fig. S1, Supporting Information). Noting that an about 2 nm dense SiO_x layer, as a functional layer to passivate the surface states, was pre-formed on the surface of all these as-prepared Si electrode by soaking in aqueous solution of H₂O₂ and HCl at 75 °C for 10 min, thus constructing a metal-insulator-semiconductor (MIS) structure when the Ni was loaded. The Si electrodes modified with continuous Ni net with various duty ratios were denoted as Si/SiO_x/yNi net ($y = 38\%, 42\%, \text{ and } 62\%$, is the duty ratio of Ni). Similarly, Si modified by the Ni dot with duty ratio of 10% and 1.5% was respectively identified as Si/SiO_x/10%Ni dot and Si/SiO_x/1.5%Ni dot. Si electrodes coated by the broken Ni net with 32% duty ratio, dense Ni film, broken Ni/NiO_x net with 32% duty ratio were denoted as Si/SiO_x/32%broken Ni net, Si/SiO_x/Ni film, and Si/SiO_x/32%broken Ni/NiO_x net, respectively. The PEC water splitting performances of these as-prepared Ni-modified Si photoanodes were measured in 1 M KOH electrolyte under AM1.5 G simulated sunlight illumination (100 mW cm⁻²). All the n-Si photoanodes with Ni modification showed much better performance than the pure n-Si photoanode without Ni layer (Fig. 3a). The saturated photocurrent density of these

Ni-modified Si electrodes increased with decreasing the coverage rate of Ni layer. The Si/SiO_x/10%Ni dot exhibited a 40 mA cm⁻² saturated current density at 1.6 V_{RHE}, which is about 2.5 times higher than the Si/SiO_x/Ni film (15 mA cm⁻² at 2.0 V_{RHE}). Moreover, the obviously higher PEC performance for the Si/SiO_x/32%broken Ni net than the Si/32% broken Ni net would indicate that the surface states of Si electrodes were effectively passivated by the pre-formed SiO_x layer.

A side experiment was carried out by patterning the Ni layer with a similar duty ratio on quartz substrate, in which light-absorption loss sharply increased with the decrease of duty ratio of Ni layer (Fig. S2, Supporting Information). The Ni layer partially covering the Si surface ensures sufficient light absorption for the photoelectrode, thus contributing to the higher PEC performances. Particularly, the photocurrents are obviously higher for the Si/SiO_x/32%Ni net than the Si/SiO_x/38% broken Ni net, while they exhibited the similar light transmissivity (92% and 93%, respectively). This phenomenon means that the charge extraction from the depletion region at the interface between MIS assembly and electrolyte is more efficient for the broken Ni net than the continuous Ni net. After depositing 15 nm-thick NiO_x on the broken Ni net, the Si/SiO_x/32% broken Ni/NiO_x net afforded a low onset potential at 0.93 V_{RHE} and 40 mA cm⁻² saturated current. As a typical example, the TEM image, high-resolution TEM image, and O, Ni, and Si element mapping were performed on the Si/SiO_x/32%broken Ni/NiO_x net and clearly visualized that the worm-like Ni/NiO_x nanoparticle formed on the surface of Si (Fig. 3b). High-resolution TEM image exhibited about 2 nm SiO_x layer on Si surface. The O element mapping clearly drew the outline of SiO_x, Ni, and NiO_x layers. These

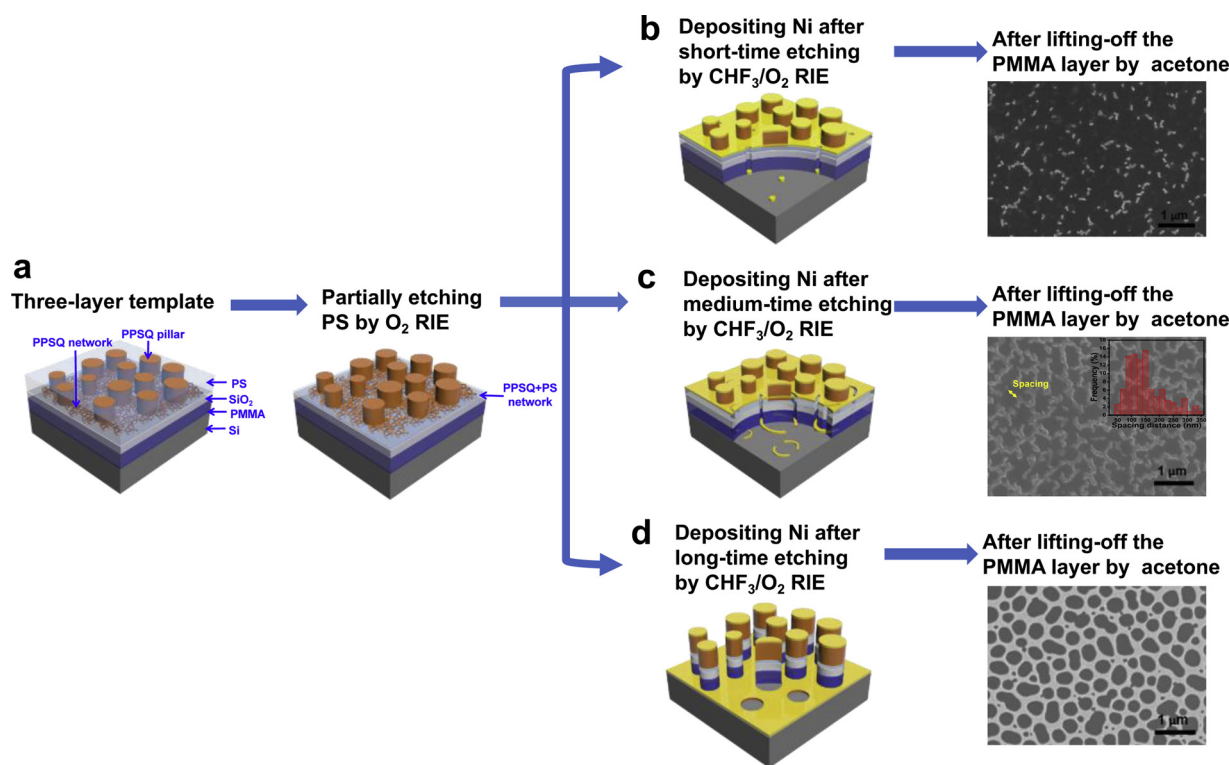


Fig. 2. a) An overlayer with the PPSQ pillars and the bicontinuous PS + PPSQ network layer was generated after partially removing PS phase from the three-layer template. b–d) SEM images for the Ni dot with duty ratio of 10%, broken Ni net with duty ratio of 32%, and Ni net with duty ratio of 38% on the Si substrate. These Ni patterns were obtained by depositing Ni after varying the etching time and subsequently lifting-off the tailored three-layer mask template. The schematic sectional drawing was used to show the internal structures of the different pores in the three-layer template and the Ni patterns on Si substrate after depositing of Ni. Inset in SEM image of Fig. 2c shows a statistical distribution of disconnected distance among these broken Ni net.

evidences demonstrated that the MIS structure was successfully constructed.

2.3. Experimental evidences to inhomogeneous barrier height inducing charge transfer

To observe the PEC difference among the Si/SiO_x/broken Ni/NiO_x net, Si/SiO_x/broken Ni net, and Si/SiO_x/Ni net electrodes with the similar light absorption, we determined the Fermi levels under equilibrium and quasi-equilibrium conditions. Hence, the open-circuit voltages under dark (OCV_{dark}) and AM 1.5 G illumination (OCV_{light}) in 1.0 M KOH electrolyte were measured. The open-circuit photovoltage (V_{ph}) is equal to $|OCV_{light} - OCV_{dark}|$, representing the flattened band bending in the depletion region from dark to light illumination [25,26]. The V_{ph} gradually increased from 200 mV (Ni net), to 220 mV (broken Ni net), and to 430 mV (broken Ni/NiO_x net) (Fig. 3c), suggesting the increased surface band bending after modification by Ni or Ni/NiO_x layer. We estimate the flat band potential (V_{fb}) of the electrodes from the Mott-Schottky plots (Fig. S3, Supporting Information), and the x -intercept of the plots gives a 0.25 V more negative V_{fb} for the Si/SiO_x/32% broken Ni net electrode (0.37 V_{RHE}) than Si/SiO_x electrode (0.62 V_{RHE}), further implying the improved band bending by Ni or Ni/NiO_x layer. Hence, compared with the Si/SiO_x/Ni net with the continuous Ni net, the enhanced V_{ph} value of Si/SiO_x/broken Ni net probably results from the inhomogeneous barrier height inducing the less charge recombination.

The charge separation efficiency increased in order of Si/SiO_x/32% broken Ni net > Si/SiO_x/32% broken Ni/NiO_x net > Si/SiO_x/38% Ni net at below 1.6 V_{RHE} (Fig. 3d). The higher charge separation efficiency for Si/SiO_x/broken Ni net than Si/SiO_x/Ni net would imply that the dispersed broken Ni net is more beneficial to generate higher Schottky barrier at the MIS-electrolyte interface than the continuous Ni net does.

After modification of NiO_x, the slightly decreased charge separation efficiency for the Si/SiO_x/broken Ni/NiO_x net than the Si/SiO_x/Ni net would originate from the slight light loss by NiO_x layer (light transmissivity, 89%). The significantly increased charge injection efficiency was observed for Si/SiO_x/broken Ni/NiO_x net than both the Si/SiO_x/Ni net and broken Si/SiO_x/Ni net. After PEC reaction on Si/SiO_x/broken Ni/NiO_x net, the Ni 2p_{3/2} XPS spectrum (Fig. S4, Supporting Information) was deconvoluted into two peaks with binding energy of 854 eV and 856.1 eV, corresponding to Ni²⁺ and Ni³⁺, respectively. The O 1s XPS spectrum was decomposed into three peaks with binding energy of 529.7 eV, 532 eV, and 532.5 eV, assigning to the lattice oxygen in NiO_x, the OH⁻ in Ni(OH)₂, and the OH⁻ in NiOOH, respectively. These evidences suggest that the Ni(OH)₂ and NiOOH, as efficient electrocatalysts, can effectively promote the OER kinetics [20,27,28]. The electrochemical impedance spectroscopy (EIS) was used to detect the interfacial charge transfer behavior. An equivalent circuit model is shown in Fig. S5 in Supporting Information. Compared to the Si/SiO_x/Ni net and broken Si/SiO_x/Ni net, the Si/SiO_x/broken Ni/NiO_x net has a lower hole transfer resistance both at the Si/SiO_x/Ni interfaces (R_{ct1}) and at MIS assembly-electrolyte interface (R_{ct2}), exhibited a strong ability for hole extraction from Si and faster OER process.

Surface potential distribution on the MIS and the Si/SiO_x regions of the Si/SiO_x/32% broken Ni net was detected by using Kelvin probe force microscope (KPFM) to measure contact potential difference (CPD) between a conducting tip and the sample. Therefore, for a semiconductor, the CPD is defined as $V_{CPD} = (\phi_{sample} - \phi_{tip})/e$ (where ϕ_{sample} and ϕ_{tip} are the work functions of the sample and tip, and e is the electronic charge), would be related to the space charge regions beneath the surfaces. As shown in Fig. 4a, it is obvious that there is about 10–80 mV higher surface potential, depending obviously on the size and inter-particle distance of Ni particles, for MIS region than Si/SiO_x region.

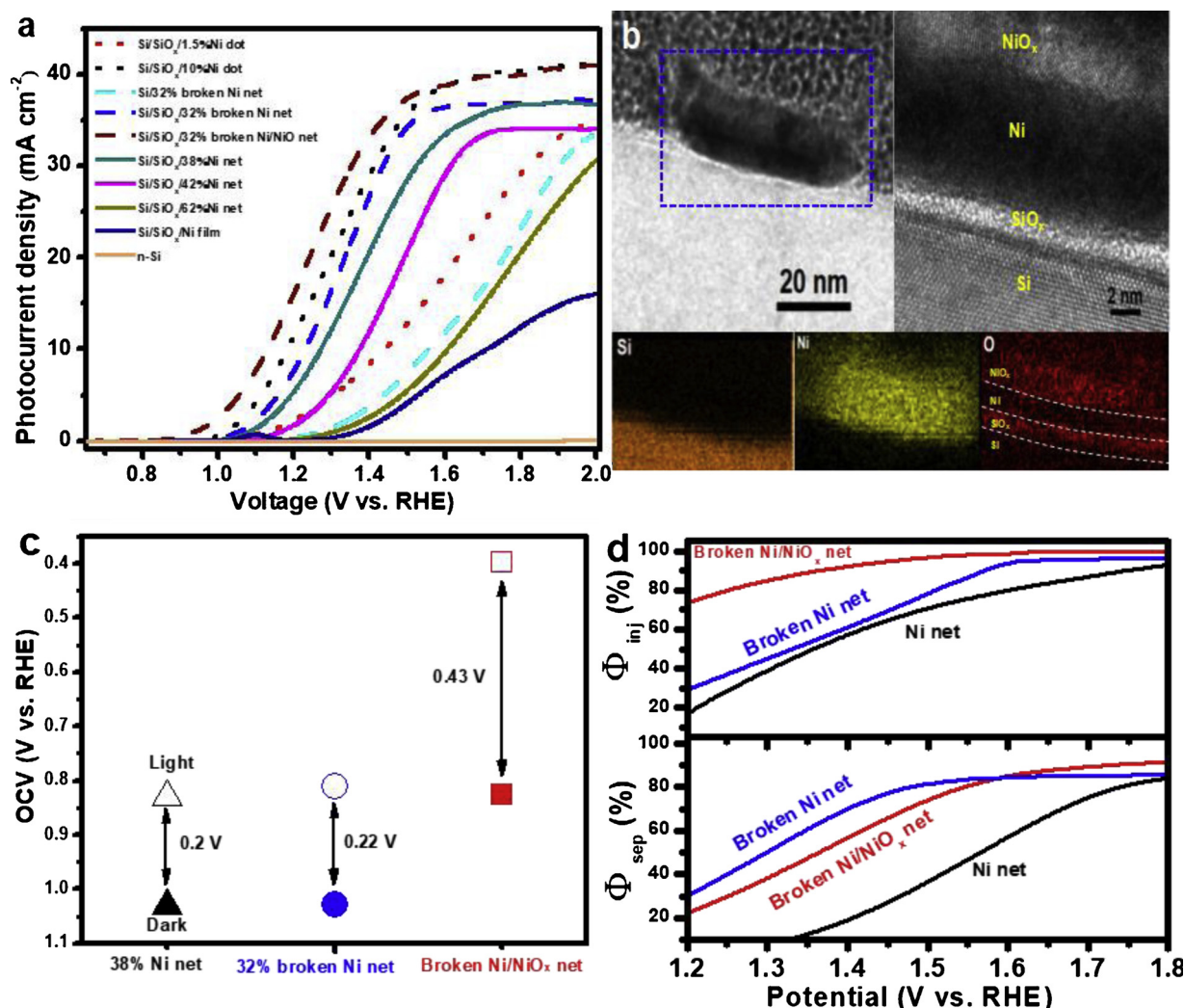


Fig. 3. a) Current-potential (J - V) curves of these as-prepared Ni-modified Si photoanodes and the n-Si photoanode under AM 1.5 G simulated sunlight (100 mW cm^{-2}) in 1 M KOH aqueous solution (scan rate 30 mV s^{-1}). b) TEM images of as-prepared Si/SiO_x/broken Ni/NiO_x net electrode. Insets show the element mapping and high-resolution TEM image observations on blue rectangular region in Fig. 3b. c) OCV of the Si/SiO_x/32%broken Ni/NiO_x net, Si/SiO_x/broken Ni net, and Si/SiO_x/Ni net electrodes. d) Charge separation and injection efficiencies for the Si/SiO_x/32% broken Ni/NiO_x net, Si/SiO_x/broken Ni net, and Si/SiO_x/Ni net electrodes.

This fact confirmed that the Ni particles are able to enlarge the surface band bending due to its high work function (4.6 eV). As a consequence, it is reasonably suggested that the higher barrier in MIS region is potentially responsible for the unusual enhancement in charge separation efficiency. After PEC reaction (Fig. 4b), the similar surface potential difference was observed, evidencing the inhomogeneous barrier height during the PEC reaction. Particularly, the Ni particles would be converted into Ni(OH)₂ and NiOOH after PEC reaction, which could provide higher work function than Ni. Thus, higher barrier could be obtained and the surface potential contrast of different area became more obvious than the sample before PEC reaction.

In theory, the V_{on} of the photoanode is strongly dependent on the V_{fb} , OER overpotential (η_k), and a potential drop across the Helmholtz layer of the electrode (η_H), following a relationship of $V_{on} = \eta_k + \eta_H + V_{fb}$ [29–33]. Evidently, the V_{on} of these Ni-modified Si photoanodes negatively shifted from $1.25 V_{RHE}$ to $1.0 V_{RHE}$ with lowering the coverage of Ni from 100% to 10% (Fig. 3a). Usually, a Si/SiO_x/Ni electrode in contact with a strongly alkaline electrolyte will form about 2 nm Ni-containing (oxy)hydroxide (a mixture of Ni(OH)₂ and NiOOH) over Ni particles. The Ni(OH)₂/NiOOH is derived from electrochemical corrosion by the strong alkaline electrolyte [34]. This fact means that these Ni modified Si electrodes may exhibit the similar η_k and η_H due to their similar MIS assembly-electrolyte interface, as demonstrated by their

similar injection efficiencies (Fig. 3d). Therefore, we consider that the Ni coverage greatly affects the V_{fb} via tuning the Schottky barrier, and hence the V_{on} . Partially covering Ni on n-type Si will produce a Schottky barrier difference between the metal covered region and the uncovered region. The higher Schottky barrier would contribute to the effective collection and injection of the hole carriers from MIS regions into electrolyte [34].

In addition, the optimized PEC performances (V_{on} and saturated current) were achieved on the Si/SiO_x/10%Ni dot and sharply decreased on the Si/SiO_x/1.5%Ni dot (Fig. 3a). This result implied that the inhomogeneous barrier height depends on the size and coverage of Ni particles. In the metal islands modified Si electrodes, the depletion layer beneath the MIS assembly can overlap if the distance between metal islands is smaller than the depletion width (W_s). The electrostatic field distribution between the islands is characterized by the smaller extension of the overlapping semispherical depletion layers, a weakening electrical field E_R perpendicular to the surface as a result of overlapping depletion layers from two adjacent metal islands [35]. For the Si/SiO_x/38%Ni net, the continuous Ni net is composed of dense aggregation of Ni nanoparticles, thus producing a strongly overlapping depletion layer (Fig. 4c). However, for the Si/SiO_x/32% broken Ni net, a statistical average 153 nm disconnected distance with the percentage of about 48% in the broken Ni net (inset of Fig. 2c) is slightly bigger

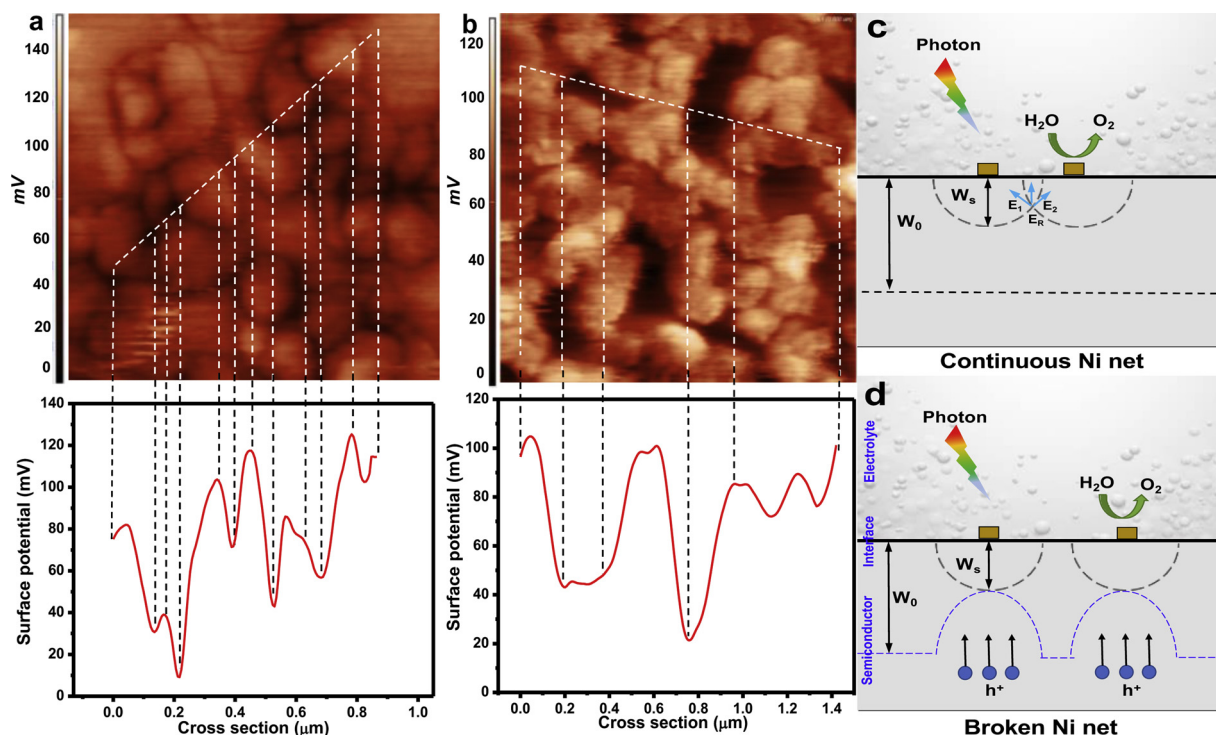


Fig. 4. KPFM images and surface potential distribution for the Si/SiO_x/32% broken Ni net a) before and b) after PEC reaction. Schematic diagram of the electrostatic field distribution in the Si electrode with c) the continuous Ni net and d) the dispersed Ni broken net. E₁ and E₂ are the electric field for two adjacent Ni islands and E_R is the electrical field perpendicular to the surface. The W_s (black dash-line semicircle) and W₀ (blue dash line and blue dash-line semicircle) respectively are the depletion width beneath the MIS region and Si/SiO_x-electrolyte interface region.

than the depletion width of Si/SiO_x electrode ($W_0 = 152$ nm at 1.23 V_{RHE}, see Fig. S3, Supporting Information, in details), effectively cutting down the electrostatic field overlapping (Fig. 4d). The region with MIS structure induces a considerably higher barrier due to the higher function work of Ni metal (4.6 eV). The hole carriers will be effectively attracted to the high barrier height locations due to the larger band bending. In the Si/SiO_x regions, the SiO_x insulation layer over the Si/SiO_x-electrolyte interface region effectively hindered the hole injection into the electrolyte, thus accumulating and tending to drift into the regions near the MIS structure. The Si/SiO_x/metal Ni junction to create a low resistance pathway for photogenerated holes, which are readily injected into the metal for OER. Enlarging the disconnected distance to the sub-micro scale will maximize the inhomogeneous barrier height effect, affording the higher PEC performance on the Si/SiO_x/10%Ni dot. The sharply decreased PEC performance on the Si/SiO_x/1.5%Ni dot would be a result of the low Ni coverage inducing inadequate MIS regions for charge collection. To check the PEC stability of Si/SiO_x/32% broken Ni@NiO_x net assembly, we ran OER at constant applied voltage of 2.3 V_{RHE} continuously for 50 h in 1.0 M K-borate electrolyte under AM 1.5 G illumination (Fig. S6, Supporting Information). The nearly constant current density of 25 mA cm⁻² was obtained, illustrating good structural and chemical stability of MIS assembly due to the fast charge collection and injection.

3. Conclusion

In summary, we proposed a novel PS + PPSQ dual-phase photoetching template with hierarchical structure, generating by a spinodal phase decomposition mechanism, to facilitate the various functional-layer patterns on Si electrodes. Such a surface functionalization method gives us a possibility to deeply understand the charge separation and transfer at semiconductor/electrolyte interface after modification by functional layers with different nanostructures. We found that isolating the high-work-function metal islands on Si surface can

efficiently collect charge as a result of effectively cutting down the electrostatic field overlapping between two adjacent metal islands. Our proposed dual-phase photoetching template route may open a new avenue to easily assemble functional layers on photoelectrodes for efficient solar energy conversion.

4. Experimental section

4.1. Materials

All the materials are commercially available and were used without further purification. Poly(methyl methacrylate) (PMMA, Mw = 990 000) and polystyrene (PS, Mw = 100 000) were obtained from Sigma-Aldrich. Polyphenylsilsequioxane (PPSQ) was purchased from Gelest, Inc. P-doped (100) n-Si wafers with a resistivity of 1–10 Ω cm⁻¹ were first cleaned using a standard RCA SC-1 procedure to remove the surface oxide layer, that is, the Si wafers were soaked in a H₂SO₄/H₂O₂ solution (3:1 V/V) for 10 min and then put into a 10 vol% aqueous solution of HF for 10 s. Subsequently, the dense SiO_x layer generated by the RCA SC-2 procedure: soaking in a solution of H₂O/concentrated HCl/H₂O₂ with a volume ratio of 5:1:1 for 10 min at 75 °C.

4.2. Preparation of Si photoanode with nanostructured Ni

The PMMA was dissolved into chlorobenzene with a 3:97 wt ratio of PMMA to chlorobenzene. The resulting solution was spin-coated on the Si substrate by Suss MicroTec Model-80RC Lithography GMBH Spin Coater with a spin speed of 3000 rpm for 40 s to obtain a 200 nm-thick PMMA layer. Subsequently, a 20 nm-thick SiO₂ layer was deposited on the PMMA layer by plasma enhanced chemical vapor deposition (PECVD, Oxford plasmalab system 80 plus). The 5%SiH₄ + 95%N₂ (V/V %) with a flowing rate of 170 sccm and N₂O with a flowing rate of 710 sccm were used as the Si and O sources, respectively. PPSQ/PS (weight ratio = 1:1) polymer blend solutions with various

concentrations were prepared by dissolving the mixture in toluene. Then, a uniform 180 nm-thick layer of the PPSQ/PS blend was spin-coated onto the SiO₂ layer under a spin speed of 3000 rpm. All the reactive-ion etching (RIE) processes were performed on an inductively coupled plasma (ICP) system (CE-300I, ULVAC). After the O₂ RIE (5 sccm, 1 Pa pressure, 30 W power), the PS constituent was selectively removed due to the high etching resistance of silicon-containing PPSQ and the PPSQ nanopillars with high aspect ratio, which were used as the first etching mask layer. The PPSQ-rich residual layer around the nanopillars was utilized as the second etching mask, the morphologies of which were variable by controlling the elimination degree of this layer. This was realized by using the CHF₃/O₂ based RIE (5/5 sccm, 1 Pa pressure, 30 W power) to etch the PPSQ-rich residual layer with various etching time. Three different etching time modes were investigated in this work. Taking the sample obtained by 4:96 solute/solvent as an example, with a short time etching mode (60 s), small holes were formed. With a medium time etching mode (120 s), disordered worm-like holes were generated. With a long time etching mode (160 s), the residual layer was totally removed, which means that the second mask no longer exists. After a subsequent two-step etching process of CHF₃/CF₄-based RIE (10/5 sccm, 1 Pa pressure, 30 W power) and O₂-based RIE (5 sccm, 1 Pa pressure, 30 W power), by using the above-mentioned layer of nanopillars and tailored residual layer as two etching masks, the nanostructures were transferred to SiO₂ and PMMA layers. The physical vapor deposition (PVD) method was then used to deposit the 5 nm Ni layers, followed by a lifting-off process with acetone by ultrasonication. Finally, Ni nanodots were achieved with the nanopillars mask and the residual layer mask in the short time etching mode, broken Ni nanonets were obtained with the nanopillars mask and the residual layer mask in the medium time etching mode and Ni nanonets were fabricated with only the nanopillars mask. To obtain the broken Ni/NiO_x nanonets, during the PVD process, the 5 nm Ni layer and the 15 nm NiO_x layer were in turn deposited with other procedures remaining the same as above-mentioned.

4.3. Characterizations

All the scanning electron microscope (SEM) images were obtained using a field-emission SEM. (ULTRA-55, ZEISS) All the transmission electron microscopy (TEM) images were obtained using a field-emission TEM (Helios Nanolab 600i, FEI). The feature sizes and the duty ratios were obtained from the SEM image by the ImageJ software. The light transmission spectra were detected using an UV-VIS-NIR spectrophotometer (UV-3600, Shimadzu) at normal incident angle.

4.4. Photoelectrochemical tests

An ohmic back contact affixed to n-Si was prepared with in particles. A Cu wire was attached to the ohmic back contact with Ag paste and packed with 704 silica gel to prevent contact with the electrolyte. All the samples were tested at room temperature in a standard three-electrode configuration with a photoanode working electrode, a Pt counter electrode, and a Ag/AgCl reference electrode, using CHI660E potentiostat. An AM1.5G sunlight simulator (100 mW cm⁻², oriel 92251A-1000) was used as light source. Potentials of the working electrode were converted to a reversible hydrogen potential (RHE) scale using the Nernst Equation:

$$E_{RHE} = E_{Ag/AgCl} + 0.059 \times pH + 0.1967V \quad (1)$$

The CHI660E potentiostat was used to measure electrochemical impedance (EIS) spectra under 10 mV amplitude perturbation and frequencies between 0.1–100000 Hz. The charge injection efficiency and charge separation efficiency were calculated through the photocurrent density obtained for the oxidation of sulfite using the methods listed in the following Eqs. (2)–(4):

$$J_{PEC} = J_{abs} \times \phi_{sep} \times \phi_{inj} \quad (2)$$

$$\phi_{inj} = \frac{J_{H_2O}}{J_{Na_2SO_3}} \quad (3)$$

$$\phi_{sep} = \frac{J_{Na_2SO_3}}{J_{abs}} \quad (4)$$

where J_{PEC} is the observed PEC photocurrent density, J_{abs} is the photocurrent density when the absorbed photons are completely converted into current, J_{H_2O} is the photocurrent density for H₂O oxidation, and $J_{Na_2SO_3}$ is the photocurrent density for Na₂SO₃.

Declaration of Competing Interest

The authors declare that they have no known competing financial interests or personal relationships that could have appeared to influence the work reported in this paper.

Acknowledgements

This work was supported primarily by the National Key R&D Program of China (2018YFB1105400), National Natural Science Foundation of China (51721001, 51872135, 51572121, 21603098, and 21633004), the Natural Science Foundation of Jiangsu Province (BK20151265, BK20151383, and BK20150580), and the Fundamental Research Funds for the Central Universities (021314380133 and 021314380084).

Appendix A. Supplementary data

Supplementary material related to this article can be found, in the online version, at doi:<https://doi.org/10.1016/j.apcatb.2019.118115>.

References

- [1] S.Y. Reece, J.A. Hamel, K. Sung, T.D. Jarvi, A.J. Esswein, J.J.H. Pijpers, D.G. Nocera, Wireless solar water splitting using silicon-based semiconductors and earth-abundant catalysts, *Science* 334 (2011) 645–648.
- [2] J.A. Turner, A nickel finish protects silicon photoanodes for water splitting, *Science* 342 (2013) 811–812.
- [3] G.M. Wang, H.Y. Wang, Y. Ling, Y.C. Tang, X.Y. Yang, R.C. Fitzmorris, C.C. Wang, J.Z. Zhang, Y. Li, Hydrogen-treated TiO₂ nanowire arrays for photoelectrochemical water splitting, *Nano Lett.* 11 (2011) 3026–3033.
- [4] R. Liu, Z. Zheng, J. Spurgeon, X.G. Yang, Enhanced photoelectrochemical water-splitting performance of semiconductors by surface passivation layers, *Energy Environ. Sci.* 7 (2014) 2504–2517.
- [5] A. Fujishima, K. Honda, Electrochemical photolysis of water at a semiconductor electrode, *Nature* 238 (1972) 37–38.
- [6] K. Sun, N. Park, Z.L. Sun, J.G. Zhou, J. Wang, X.L. Pang, S.H. Shen, S.Y. Noh, Y. Jing, S. Jin, P.K.L. Yu, D. Wang, Nickel oxide functionalized silicon for efficient photo-oxidation of water, *Energy Environ. Sci.* 5 (2012) 7872.
- [7] Z.B. Luo, T. Wang, J.L. Gong, Single-crystal silicon-based electrodes for unbiased solar water splitting: current status and prospects, *Chem. Soc. Rev.* 48 (2019) 2158–2181.
- [8] J.H. Zhao, T.M. Gill, X.L. Zheng, Enabling silicon photoanodes for efficient solar water splitting by electroless-deposited nickel, *Nano Res.* 11 (2018) 3499–3508.
- [9] M.F. Lichterman, K. Sun, S. Hu, X.H. Zhou, M.T. McDowell, M.R. Shaner, M.H. Richter, E.J. Crumlin, A.I. Carim, F.H. Saadi, B.S. Brunswig, N.S. Lewis, Protection of inorganic semiconductors for sustained, efficient photoelectrochemical water oxidation, *Catal. Today* 262 (2016) 11–23.
- [10] K. Sun, F.H. Saadi, M.F. Lichterman, W.G. Hale, H.P. Wang, X. Zhou, N.T. Plymale, S.T. Omelchenko, J.H. He, K.M. Papadantonakis, B.S. Brunswig, N.S. Lewis, Stable solar-driven oxidation of water by semiconducting photoanodes protected by transparent catalytic nickel oxide films, *Proc. Natl. Acad. Sci. U. S. A.* 112 (2015) 3612–3617.
- [11] X.H. Zhou, R. Liu, K. Sun, K.M. Papadantonakis, B.S. Brunswig, N.S. Lewis, 570 mV photovoltage, stabilized n-Si/CoO_x heterojunction photoanodes fabricated using atomic layer deposition, *Energy Environ. Sci.* 9 (2016) 892–897.
- [12] M.J. Kenney, M. Gong, Y.G. Li, J.Z. Wu, J. Feng, M. Lanza, H.J. Dai, High-performance silicon photoanodes passivated with ultrathin nickel films for water oxidation, *Science* 342 (2013) 836–840.
- [13] K. Sun, S.H. Shen, J.S. Cheung, X.L. Pang, N. Park, J.G. Zhou, Y.F. Hu, Z.L. Sun, S.Y. Noh, C.T.J. Riley, P.K.L. Yu, Si photoanode protected by a metal modified ITO layer with ultrathin NiO_x for solar water oxidation, *Phys. Chem. Chem. Phys.* 16 (2014) 4612–4625.

- [14] X.W. Yu, P. Yang, S. Chen, M. Zhang, G.Q. Shi, NiFe alloy protected silicon photoanode for efficient water splitting, *Adv. Energy Mater.* 7 (2017) 1601805.
- [15] G. Loget, B. Fabre, S. Fryars, C. Mériadec, S. Ababou-Girard, Dispersed Ni nanoparticles stabilize silicon photoanodes for efficient and inexpensive sunlight-assisted water oxidation, *ACS Energy Lett.* 2 (2017) 569–573.
- [16] R.C. Rossi, N.S. Lewis, Investigation of the size-scaling behavior of spatially non-uniform barrier height contacts to semiconductor surfaces using ordered nanometer-scale nickel arrays on silicon electrodes, *J. Phys. Chem. B* 105 (2001) 12303–12318.
- [17] S.A. Lee, T.H. Lee, C. Kim, M.G. Lee, M.J. Choi, H. Park, S. Choi, J. Oh, H.W. Jang, Tailored NiO_x/Ni cocatalysts on silicon for highly efficient water splitting photoanodes via pulsed electrodeposition, *ACS Catal.* 8 (2018) 7261–7269.
- [18] J.C. Hill, A.T. Landers, J.A. Switzer, An electrodeposited inhomogeneous metal-insulator-semiconductor junction for efficient photoelectrochemical water oxidation, *Nat. Mater.* 14 (2015) 1150.
- [19] C.L. Li, M. Huang, Y.J. Zhong, L. Zhang, Y.Q. Xiao, H.W. Zhu, Highly efficient NiFe nanoparticle decorated Si photoanode for photoelectrochemical water oxidation, *Chem. Mater.* 31 (2018) 171–178.
- [20] G.Z. Xu, Z. Xu, Z. Shi, L. Pei, S.C. Yan, Z.B. Gu, Z.G. Zou, Silicon photoanodes partially covered by Ni@Ni(OH)₂ core-shell particles for photoelectrochemical water oxidation, *ChemSusChem* 10 (2017) 2897–2903.
- [21] Y. Li, K. Hu, X. Han, Q.Y. Yang, Y.F. Xiong, Y.H. Bai, X. Guo, Y.S. Cui, C.S. Yuan, H.X. Ge, Phase separation of silicon-containing polymer/polystyrene blends in spin-coated films, *Langmuir* 32 (2016) 3670–3678.
- [22] M. Böltau, S. Walheim, J. Mlynek, G. Krausch, U. Steiner, Surface-induced structure formation of polymer blends on patterned substrates, *Nature* 391 (1998) 877.
- [23] R.A. Jones, L.J. Norton, E.J. Kramer, F.S. Bates, P. Wiltzius, Surface-directed spinodal decomposition, *Phys. Rev. Lett.* 66 (1991) 1326.
- [24] K. Tanaka, A. Takahara, T. Kajiyama, Film thickness dependence of the surface structure of immiscible polystyrene/poly (methyl methacrylate) blends, *Macromolecules* 29 (1996) 3232–3239.
- [25] N.S. Lewis, A quantitative investigation of the open-circuit photovoltage at the semiconductor/liquid interface, *J. Electrochem. Soc.* 131 (1984) 2496–2503.
- [26] A. Zaban, M. Greenshtein, J. Bisquert, Determination of the electron lifetime in nanocrystalline dye solar cells by open-circuit voltage decay measurements, *ChemPhysChem* 4 (2003) 859–864.
- [27] O. Diaz-Morales, D. Ferrus-Suspedra, M.T.M. Koper, The importance of nickel oxyhydroxide deprotonation on its activity towards electrochemical water oxidation, *Chem. Sci.* 7 (2016) 2639–2645.
- [28] L.Y. He, W. Zhou, D.P. Cai, S.S. Mao, K. Sun, S.H. Shen, Pulsed laser-deposited n-Si/NiOx photoanodes for stable and efficient photoelectrochemical water splitting, *Catal. Sci. Technol.* 7 (2017) 2632–2638.
- [29] Y.V. Pleskov, *Solar Energy Conversion: A Photoelectrochemical Approach*, Springer, New York, 1990.
- [30] M. Barroso, S.R. Pendlebury, A.J. Cowan, J.R. Durrant, Charge carrier trapping, recombination and transfer in hematite (α -Fe₂O₃) water splitting photoanodes, *Chem. Sci.* 4 (2013) 2724–2734.
- [31] B. Iandolo, H.X. Zhang, B. Wickman, I. Zorić, G. Conibeer, A. Hellman, Correlating flat band and onset potentials for solar water splitting on model hematite photoanodes, *RSC Adv.* 5 (2015) 61021–61030.
- [32] M.G. Walter, E.L. Warren, J.R. McKone, S.W. Boettcher, Q.X. Mi, E.A. Santori, N.S. Lewis, Solar water splitting cells, *Chem. Rev.* 110 (2010) 6446–6473.
- [33] C. Du, X.G. Yang, M.T. Mayer, H. Hoyt, J. Xie, G. McMahon, G. Bischofing, D.W. Wang, Hematite-based water splitting with low turn-on voltages, *Angew. Chem. Int. Ed.* 52 (2013) 12692–12695.
- [34] F.A.L. Laskowski, M.R. Nellist, R. Venkatkarthick, S.W. Boettcher, Junction behavior of n-Si photoanodes protected by thin Ni elucidated from dual working electrode photoelectrochemistry, *Energy Environ. Sci.* 10 (2017) 570–579.
- [35] H.J. Lewerenz, Operational principles of electrochemical nanoemitter solar cells for photovoltaic and photoelectrocatalytic applications, *J. Electroanal. Chem.* 662 (2011) 184–195.